MATERIALS PHYSICS AND MECHANICS RESEARCH ARTICLE

Submitted: December 13, 2024 **Revised: January 30, 2024** **Accepted: February 18, 2025**

Multifractal properties of breaking bonds coordinates in heterogeneous materials revealed by the discrete element method

V.L. Hilarov ✉, **E.E. Damaskinskaya**

Ioffe Institute, St. Petersburg, Russia

✉ vladimir.hilarov@mail.ioffe.ru

ABSTRACT

Using the discrete element method coordinates of elementary acoustic emission sources (breaking bonds) were calculated as a function of time for materials of different degrees of heterogeneity under mechanical loading. The time dependences of multifractal dimension spectra $D(q)$ for these sources were calculated using the "sandbox" algorithm. The time behavior of spectra width w and box counting fractal dimension D_0 was studied. A narrowing of the multifractal dimension spectra was discovered (fractal self-organization of acoustic emission) before the destruction of materials and its subsequent expansion after the formation of a main crack. The influence of physical properties of the polycrystalline grain boundaries on the strength and ductility of materials has been revealed.

KEYWORDS

fracture of materials • discrete element method • multifractals • self-organization

Citation: Hilarov VL, Damaskinskaya EE. Multifractal properties of breaking bonds coordinates in heterogeneous materials revealed by the discrete element method. *Materials Physics and Mechanics*. 2025;53(1): 38–47.

http://dx.doi.org/10.18149/MPM.5312025_3

Introduction

The discrete element method (DEM) has recently been widely used to study the nature of solids fracture [1–11]. Its advantage over traditional continuum methods for calculating mechanical properties, such as finite element method (FEM) [12–14] is that it naturally takes into account discontinuities in materials. The material is specified by a set of particles of various shapes that simulate polycrystalline grains and bonds between these particles at the points of their contacts (BPM is a bonded particle model) [15]. We used spherical particles.

The advantage of the DEM method for calculating multifractal characteristics is that the coordinates of all broken bonds are known with great accuracy, which makes it possible to calculate spatial fractal characteristics directly based on these coordinates. In all laboratory acoustic emission (AE) experiments and field observations of seismic events, only a small part of the acoustic signals is recorded, and the coordinates of the signal sources are calculated from the spatial location of the sensors receiving these signals. When using the DEM method, such a procedure is not necessary.

Though there are many papers concerning DEM, we found none devoted to the analysis of the change in multifractal spectra in the fracture process of materials. Meanwhile, these investigations seem to be very important since multifractal self-organization can serve as a precursor of materials destruction in the fracture process [16–19]. Moreover, there are significant reasons to believe that fractal self-organization

Publisher: Peter the Great St. Petersburg Polytechnic University

is a common feature of disasters of various nature [17–23]. The presence of the same peculiarities in very different systems suggests that these peculiarities are not connected with the details of the system elements interaction but rather with the character of these elements collectivization. That is why the present study appears to be actual and noteworthy. Calculations using the discrete element method were carried out using the freely available MUSEN software package [24].

Computer simulation

Though the experimental scheme considered in this paper is similar to that described in [25], the quantities analyzed in the current study and discussed further are quite different from those in [25]. In that paper we analyzed stresses and acoustical signal distributions, while the present paper is devoted to the analysis of multifractal features of acoustic emission (AE) sources. Cylindrical samples with a diameter of 10 mm and a height of 20 mm were modeled. Cylinders were filled with spherical particles of the same or different sizes and packed until a porosity of 0.35–0.37 was reached. Particles and bonds between them (grains and grain boundaries) were assumed to be made of the materials listed in Table 1.

Though the parameters used are characteristic of granites, it should be noted that "microscopic" values of parameters for the particles and bonds result in different values for real material parameters. That is why calibration of the "microscopic" parameters is required to compare the values of the mechanical properties of the modeling materials with the real ones [15]. As this paper has not had the task to compare numerical values of the magnitudes for the modeled and real materials (for example, a strength thereof), such parameter calibration was not carried out.

Table 1. Material properties used in the simulation

#	Material	ρ, kg/m^3	E, GPa	ν	σ_n, MPa	σ_t, MPa	η, Pa · s
1	Quartz	2650	94	0.29	600	600	5E19
2	Orthoclase	2560	62	0.29	420	420	1E19
3	Oligoclase	2560	70	0.29	480	480	1E19
4	Glass	2500	50	0.22	50	50	1E40
5	Quartz-orthoclase bonds	2500	5.8	0.2	200	200	5E19
6	Quartz-oligoclase bonds	2500	5.8	0.2	300	300	5E19
7	Orthoclase-oligoclase bonds	2500	5.8	0.2	100	100	5E19

Here, ρ is the density of material, E is Young's modulus, ν is Poisson's ratio, σ_n is normal strength, σ_t is shear strength, η is dynamic viscosity.

Four types of samples were used: two samples contained particles connected with orthoclase bonds. Diameters of these bonds in sample 1 were $d = 0.04$ mm and in sample 2 $d = 0.1$ mm. Grains (particles) in these samples had diameters and composition shown in Tables 2 (sample 2) and 3 (sample 1). For the sample 1 diameters were normally distributed with a mean value of 0.08 mm and a standard deviation of 0.025 mm. The diameter of fraction 4 for orthoclase was increased 10 times in order to increase the degree of heterogeneity. For the sample 2 diameters are normally distributed, with a mean value of 0.3 mm and a standard deviation of 0.1 mm obtained by a random number generator with a normal distribution. Sample 1 and sample 2 have 33670 and 48695 particles, respectively.

Sample 3 contained particles with diameters and composition shown in Table 3 (the number of particles is 33670). Particle diameters were the same as for sample 1. In this sample, bonds of the same material connected particles made from the same material, while glass bonds 4 from Table 1 connected particles from different materials. Bond diameters in this sample were $d \leqslant 0.1$ mm.

Table 2. Particles diameters and composition for each fraction

	Particles diameters for each fraction d_i, mm					The relative content of each fraction
Quartz	0.36	0.188	0.52	0.28	0.42	0.0595745
Orthoclase	0.27	0.28	0.4	0.36	0.26	0.0702128
Oligoclase	0.16	0.168	0.288	0.24	0.4	0.0702128

Table 3. Particles diameters and composition for each fraction

	Particles diameters for each fraction d_i, mm					The relative content of each fraction
Quartz	0.09	0.047	0.132	0.079	0.106	0.0595745
Orthoclase	0.068	0.07	0.096	0.91	0.064	0.0702128
Oligoclase	0.041	0.042	0.077	0.063	0.098	0.0702128

Sample 4 had the same composition as sample 2. Bonds from the same material connected particles from the same material, while low-modulus bonds 5–7 (Table 1) with diameters $d \leqslant 0.6$ mm connected particles from different materials.

For samples 2, 3 and 4, the bond diameters (d) were chosen by the MUSEN program bond generator to be equal to the smaller diameter of the pair of connected particles 1 and 2: $d = \min\{d_1, d_2\}$ [24].

Samples were placed in a virtual press. The lower plate was fixed, and the upper one moved down with a constant speed $v = 0.02$ m/s until the sample was destroyed. Thus, uniaxial compression was simulated. Since $v = 0.02$ m/s and the height of the sample is 0.02 m, the axial strain $\varepsilon = v \cdot t/h$ and time are numerically equal.

A large set of different mechanical parameters was recorded during the deformation of the samples. In the present work, these parameters were the lifetimes of broken bonds and their space coordinates. Each breaking of the bond is considered in this study to be an elementary acoustic emission event.

The following algorithm has been used in order to calculate the multifractal properties of the coordinates of acoustic emission (AE) centers. The entire time series of these coordinates (AE signals) was divided into successive samples of 4096 events. The time value was assigned to the time of the last sampling event. For each such sample, the multifractal dimension spectrum (MDS) was calculated using the "sandbox" algorithm [26–28]. According to this method, the generalized fractal dimension D_q is defined as: $D_q = \lim\limits_{r \to 0} \frac{ln<(M_i(r)/N)^{q-1}>}{\ln (r/d)} \cdot \frac{1}{q-1}$, where d is the spatial size of the multifractal set, $M_i(r)$ is the number of AE signals emitted inside a sphere of radius r centered at the point of the i-th event, q is the scaling moment. Angle brackets indicate statistical averaging over randomly selected points. Due to the small size of the sets under study ($N = 4096$ events), all points of the set were taken into account in this work.

In practice, the scaling exponents $\tau(q)$ are first determined by linear regression of $lnS = ln < (M_i(r)/N)^{q-1} >$, constructed as a function of $\ln(r/d)$. After that, the multifractal dimension spectrum $D_q = \tau(q)/(q-1)$ for $q \neq 1$ has been estimated. A uniform sequence of 21 numbers in the range [-5 – +5] was used as the set q. We did not calculate the information dimension D_1 in this work. Only parameters D_0 and $w = D_{-5} - D_5$ were used (the box counting fractal dimension and spectrum width).

No special choice for the points near the border of the sample was used. This led to boundary effects. However, it is well known that these effects violate the linear dependence of the statistical sum logarithm on the logarithm of scale on large scales. Therefore, nonlinearity on these scales was simply withdrawn from the regression.

The typical scaling dependence of $lnS = ln < (M_i(r)/N)^{q-1} >$, on $\ln(r)$ and the multifractal dimension spectrum $D_q = \tau(q)/(q-1)$ are shown in Fig. 1. Nonlinear regions on small and large scales were omitted during regression.

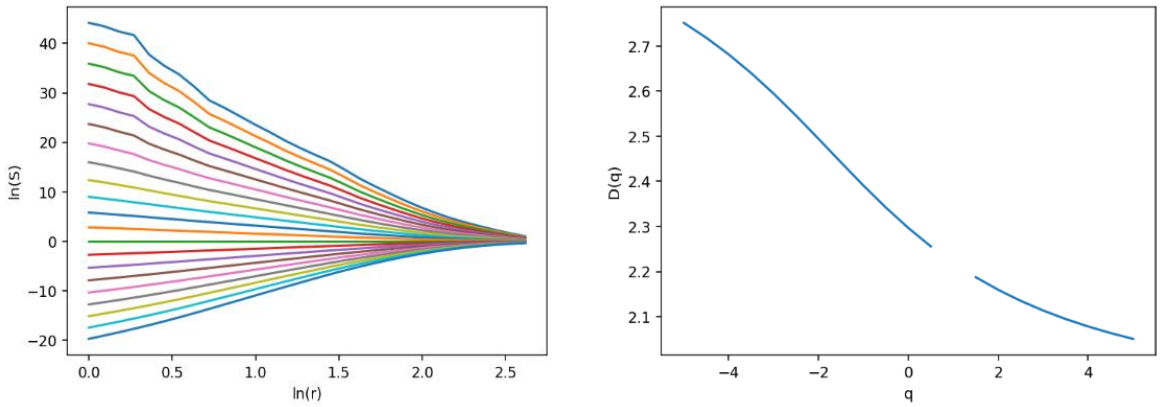

(a) (b)

Fig. 1. Typical scaling dependence of $\ln S = \ln < (M_i(r)/N)^{q-1} >$ on $\ln(r)$ and the multifractal spectrum $D(q)$

Main results

Figure 2 shows the loading diagram (the stress-strain curve), as well as the multifractal parameters D_0 (box counting fractal dimension) and w (the width of the multifractal dimension spectrum MDS) as functions of time for sample 1 with orthoclase bonds.

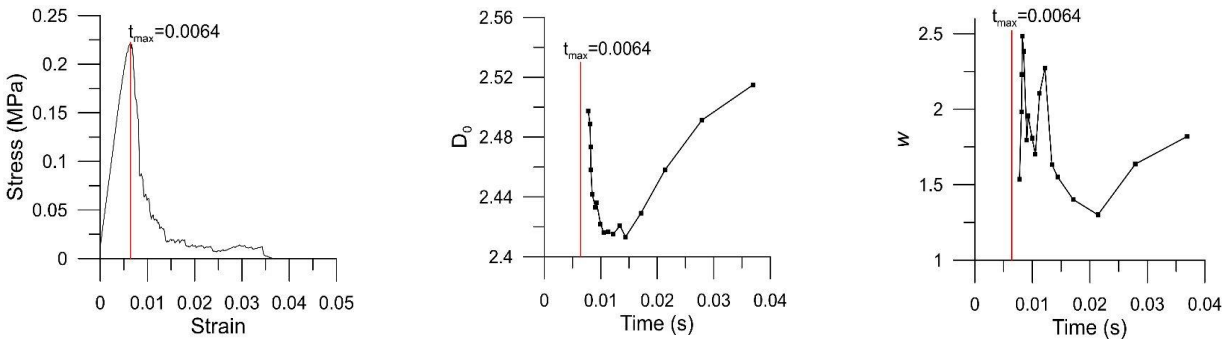

(a) (b) (c)

Fig. 2. Loading diagram (a) and time dependences of the fractal dimension (b) and the width of the multifractal dimension spectrum (c) of sample 1. Strain and time are numerically equal

Near time point $t \approx 0.01$ s, a source of destruction was formed [24], which subsequently evolved until the fracture of the entire sample occurred. Before its formation, both the fractal dimension D_0 and the spectral width w decreased. Vertical straight lines correspond to the maximum of the loading diagram at the time point $t = t_{max}$. There are not enough acoustic signals (bond breaking events) in order to calculate multifractal parameters in the pre-peak region.

Figure 3 shows similar dependences for an even more homogeneous sample 2, all bonds of which had the same thickness d = 0.1 mm. Vertical straight lines correspond to the maximum load on the loading diagram and the moment of failure of the sample when this load decreases to zero. Acoustic emission characteristics are given starting from the time point of about $t \approx 0.014$ s, because up to this point, AE is practically absent. Before destruction, a decrease in the w is again observed. It slightly decreases before $t \sim t_{max}$ and sharply decreases just before the fracture time t_f (where the stress acting on the loading plane of the loading diagram approaches zero). It can be noted that immediately at the moment of destruction these parameters increase sharply. After this sample's destruction fragments hit the loading plates, so the breakdown continues. The multifractal spectrum parameters in this time range have no physical sense.

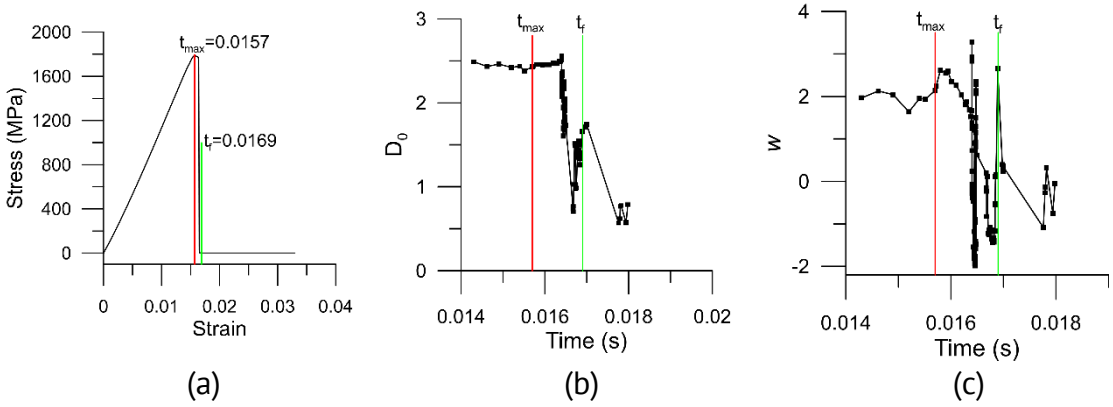

Fig. 3. Loading diagram (a) and time dependences of the fractal dimension (b) and the width of the multifractal dimension spectrum (c) of sample 2. Strain and time are numerically equal

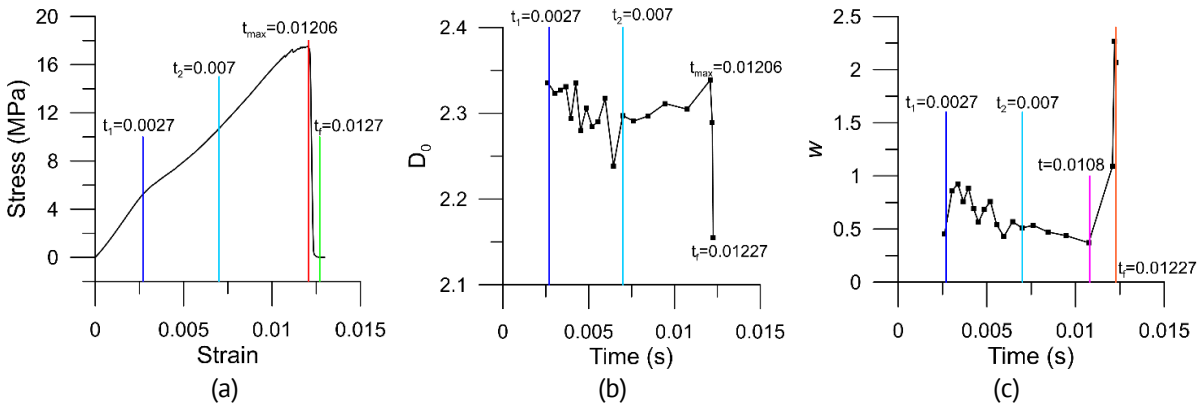

Fig. 4. Loading diagram (a) and time dependences of the fractal dimension (b) and the width of the multifractal dimension spectrum (c) of sample 3

Figure 4 depicts the multifractal characteristics of sample 3, containing low-strength glass bonds (#4 Table 1). One should notice that the loading diagram in this case becomes nonlinear. In the time interval $t \approx 0.0027-0.007$ s, the slope of this diagram changes. In this time range, an increase in the number of glass bond breaks is observed. Thus, the presence of glass bonds in the sample leads to its "quasi-plasticity" – the nonlinear character of the loading diagram caused by the glass bonds breakdown. Rather chaotic changes in multifractal characteristics D_0 and w occur during this time. When most of the glass bonds have broken, the slope of the loading diagram increases again while D_0 increases, and w decreases. During the sample destruction, there is a sharp downward jump in D_0 and an increase in w.

Figure 5 shows the multifractal parameters of sample 4, in which low-modulus bonds from Table 1 connected particles of different materials. The loading diagram has an almost horizontal section (shelf) for quite a long time (the loading speed was chosen in such a way that the deformation value and the time reference were numerically the same). During this time, the bonds between particles of the same materials are predominantly broken. The value of D_0 in this time range is quite high and does not change significantly. The spectrum width w also changes little and is very small in magnitude, i.e. the system is practically monofractal. During the destruction, there is a sharp decrease in D_0 and after it an increase in the spectrum width w.

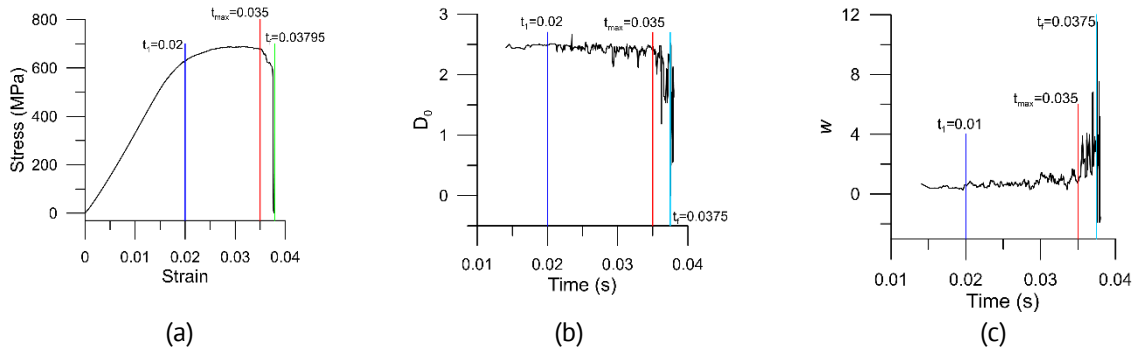

Fig. 5. Loading diagram (a) and time dependences of the fractal dimension (b) and the width of the multifractal dimension spectrum (c) of sample 4

Discussion

It is obvious that homogeneous samples 1 and 2 are destroyed in a brittle manner, as it follows from Figs. 2 and 3. Moreover, almost from the very beginning of deformation, a crack is formed in sample 1, which subsequently evolves [29]. Before its formation, the fractal dimension and spectral width w decrease. Sample 2 elastically deforms before crack formation, which is reflected in the linear dependence of stress on strain. Before the formation of the crack, a decrease in the spectrum width w is also observed. However, after the formation of the main crack, an increase in these parameters is seen in both samples. Similar dependencies were discovered in the surface profile transformation while deforming thin metal foils, for example [16,17]. After the formation of a main crack in these experiments, the widths of the multifractal singularity spectra increased, and it was hypothesized that this occurred because of stress relaxation caused by the formation of a main crack. Here we confirm this hypothesis, since the stress relaxation is directly

observed in the form of a sharp decrease in stress in the loading diagrams after the crack formation. The images of cracks discussed here are shown below.

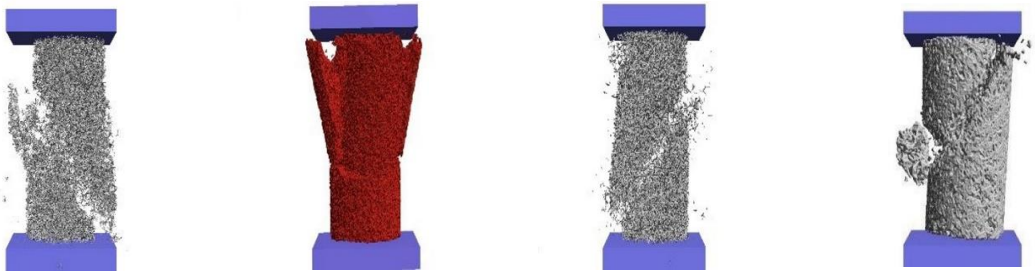

Fig. 6. Paterns of destruction for samples 1 (a), 2 (b), 3 (c) and 4 (d)

In heterogeneous sample 3 the loading diagram is nonlinear in the time range (t_1,t_2). In this time range, mainly low-strength glass bonds are broken. The restoration of the elastic modulus at $t > t_2$ may be explained by the fact that in this time range, the rate of destruction of glass bonds significantly decreases while the rate of other bonds type breakage is not yet very high (Fig. 7(a)). Thus, the cause of stress relaxation in this case is the breakage of the glass bonds. The width of the multifractal dimension spectrum w decreases before the sample destruction, whereas the fractal dimension D_0 sharply decreases only during this destruction.

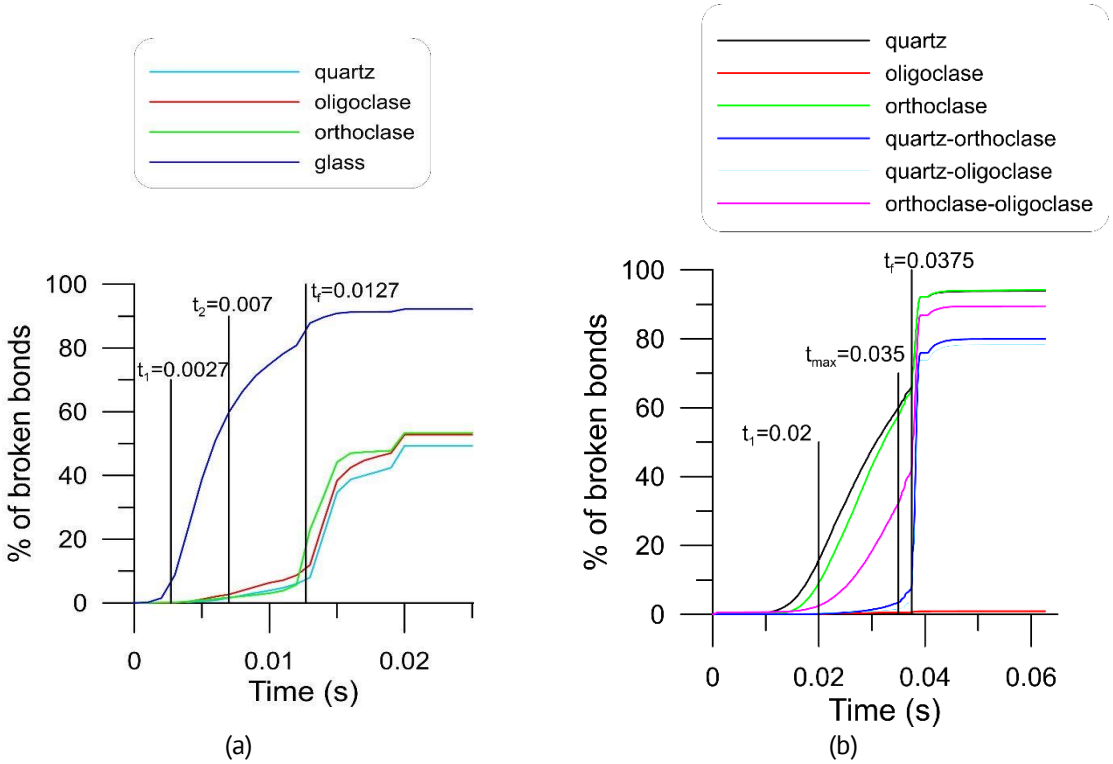

Fig. 7. Kinetics of different bonds types: (a) sample 3 with the "glass bonds", (b) sample 4 with low elastic modulus bonds

The nonlinearity of the loading diagram at $t > t_1$ for the sample 4 may be explained by the fact that in this time range the rate of rupture of high-strength bonds (1 – 3 from Table 1) reaches a maximum. The weaker bonds (5 – 7) remain mainly intact due to their deformation ability because of the low elastic modulus (Fig. 7(b)). Thus, in this case, the rupture of high-modulus strong bonds causes the stress relaxation. The fractal dimension D_0 experiences a sharp jump, and the spectrum width w sharply increases after the main crack formation $t > t_f$ due to the increased relaxation of mechanical stresses.

Similar loading diagrams and multifractal characteristics were observed in a laboratory research [30] on the fracture process in Westerly granite samples. Defect formation was monitored by recording acoustic emission (AE) signals. In these experiments, the monofractality of the AE centers was held until the moment of sample destruction, and the correlation fractal dimension $\boldsymbol{D_2}$ decreased before this destruction [31]. Loading feedback took place in the laboratory experiments: the loading system reduced the external load if the acoustic activity exceeded a specified threshold. Thus, the loading system itself simulates stress relaxation. However, unlike a computer simulation, this feedback made it possible to significantly extend the time of the fracture process. Therefore, the time range of $\boldsymbol{D_2}$ decrease in the laboratory experiment is significantly larger.

The nonlinearity of the loading diagram before the catastrophic stress decrease in heterogeneous samples can be explained in the computer simulations under consideration in two ways. The first one is the "quasi-plastic" deformation, the whose role of in sample 3 plays the breakage of low-strength glass bonds, and in sample 4 the breakage of high-modulus strong bonds. Secondly, in sample 3 this nonlinearity can be caused by intergranular fracture, since here the brittle bonds connecting grains of different materials are destroyed. While in sample 4 this nonlinearity is associated with intragranular fracture, since in this time range bonds connecting grains of the same materials are destroyed. In this case, the formation of a macro crack and the final destruction of the sample can be explained by intergranular destruction (the destruction of grain boundaries).

The mechanical strength of sample 4 is significantly higher than that of a similar sample with glass bonds of the same geometry (700 and 300 MPa), and the fracture strains are also significantly higher (0.037 and 0.015). Loading diagram for the glass bond sample is given in [25]. Since these samples have the same particle composition and differ only in the materials of intergranular bonds, it can be concluded that materials with the possibility of intergranular deformation have higher ductility compared to materials with rigid grain boundaries. The mechanical strength of materials is also determined by the strength of grain boundaries (intergranular bonds connecting particles of different materials, taking into account their diameter). The higher the strength of these boundaries, the higher the strength of the material as a whole.

The meaning of the decrease in the fractal dimension before the fracture occurs can be explained by the localization of the process with the crack formation at the late stage of the fracture process [31]. Breaking bonds start to form the crack, whose fractal dimension is close to that of the plane. The macro cracks are usually monofractal; that is why the width of the multifractal spectra decreases before crack formation.

Conclusion

Thus, the character of the fracture process changes in time while approaching destruction from the more complicated (stochastic, multifractal) to a more simple – monofractal one. A decrease in the width of the multifractal dimension spectra before the destruction of the material indicates the fractal self-organization of the process. We believe that this self-organization is a result of self-organized criticality like dynamics of the system. The obtained results could be used in detecting onset of failure of heterogeneous materials.

CRediT authorship contribution statement

Vladimir Hilarov **:** conceptualization, methodology, software, writing - original draft, supervision, **Ekaterina Damaskinskaya** **:** writing - review & editing, visualization, investigation.

Conflict of interest

The authors declare that they have no conflict of interest.

References

1. Hazzard JF, Young RP. Simulating Acoustic Emissions in Bonded-Particle Models of Rock. *Int J Rock Mech Min Sci*. 2000;37(5): 867–872.
2. Hofmann H, Babadagli T, Zimmermann G. A grain based modeling study of fracture branching during compression tests in granites. *Int J Rock Mech Min Sci*. 2015;77: 152–162.
3. Vora HB, Morgan JK. Microscale Characterization of Fracture Growth and Associated Energy in Granite and Sandstone Analogs: Insights Using the Discrete Element Method. *J Geophys Research: Solid Earth*. 2019;124(8): 7993–8012.
4. Cho N, Martin CD, Sego DC. A clumped particle model for rock. *Int J Rock Mech Min Sci*. 2007;44(7): 997–1010.
5. Hazzard JF, Young RP. Moment tensors and micromechanical models. *Tectonophysics*. 2002;356(1–3): 181–197.
6. Zhang XP, Wong LNY. Cracking Processes in Rock-Like Material Containing a Single Flaw Under Uniaxial Compression: A Numerical Study Based on Parallel Bonded-Particle Model Approach. *Rock Mech and Rock Engineering*. 2012;45: 711–737.
7. Lisjak A, Grasselli G. A review of discrete modeling techniques for fracturing processes in discontinuous rock masses. *J of Rock Mech. and Geotechnical Engineering*. 2014;6(4): 301–314.
8. Shunying Ji and Shaocheng D. Discrete element modeling of acoustic emission in rock fracture. *Theor & Appl Mech Lett*. 2013;3(2): 021009.
9. Lu JM, Li CF, Cao GC, Hu SM. Simulating Fractures with Bonded Discrete Element Method. *IEEE Transactions on Visualization and Computer Graphics*. 2022;28(12): 4810–4824
10. Munkholm L, Balling O, Serban R, Negrut D, Heck R, Green O. Modeling soil aggregate fracture using the discrete element method. *Soil and Tillage Research*. 2022;218: 105295
11. Tomac I, Gutierrez M. Micromechanics of hydraulic fracturing and damage in rock based on DEM modeling. *Granular Matter*. 2020;22: 56.
12. Segerlind L. *Applied Finite Element Analysis*. John Wiley & Sons Inc; 1984.
13. Erhunmun E., Ikponmwosa U. Review on Finite Element Method. *Journal of Applied Sciences and Environmental Management*. 2017;21(5): 999–1002.
14. Borovkov AI, Maslov LB, Zhmaylo MA, Tarasenko FD, Nezhinskaya LS. Finite element analysis for prediction of femoral component strength in hip joint endoprosthesis made from meta-biomaterial. *Materials Physics and Mechanics*. 2024;52(6): 38–60.
15. Potyondy DO, Cundall PA. A bonded-particle model for rock. *Int J Rock Mech Min Sci*. 2004;41(8): 1329–1364.

16. Korsukov VE, Ankudinov AV, Betekhtin VI, Butenko PN, Verbitskii VN, HilarovVL, Hilarov IV, Knyazev SA, Korsukova MM, Obidov BA. Dynamics of the surface morphology of a tungsten foil under load. *Phys. Solid State*. 2020;62: 2249–2257.
17. Obidov BA, Korsukov VE, Hilarov VL, Ankudinov AV, Butenko PN, Knyazev SA, Korsukova MM. Multifractal properties of the molybdenum ribbon surface at mechanical loading. *Phys. Solid State*. 2022;64: 925–928.
18. Gibowicz SJ, Lasocki S. Seismicity induced by mining: Ten years later. *Advances in Geophysics*. 2001;44: 39–181.
19. Kasimova VA, Kopylova GN, Lyubushin AA. Variations in the Parameters of Background Seismic Noise during the Preparation Stages of Strong Earthquakes in the Kamchatka Region. *Izvestiya Physics of the Solid Earth*. 2018;53: 269–283.
20. Ivanov PCh, Amaral NLA., Goldberger AL, Havlin S, Rosenblum MG, Struzikk ZR, Stanley HE. Multifractality in human heartbeat dynamics. *Nature*. 1999;399: 461–465.
21. Jiang J-Q, Xie W-J, Zhou W-X, Sornette D. Multifractal analysis of financial markets: a review. *Rep Prog Phys*. 2019;82(12): 125901.
22. Hilarov VL. On the fractal self-organization of the financial time series. *J Digit Sci*. 2022;4(1): 71-77.
23. Zhukov S. Personality and Society in the Theory of Self-Organized Criticality. *Changing Societies & Personalities*. 2023;7(2): 10–33.
24. Dosta M, Skorych V. MUSEN: An open-source framework for GPU-accelerated DEM simulations. *SoftwareX*. 2020;12: 100618.
25. Hilarov VL, Damaskinskaya EE. Modeling of fracture and acoustic emission in polycrystalline solids with the discrete elements method. *Phys Sol. State*. 2022;64(6): 664–669.
26. Tél T, Fulop A, Vicsek T. Determination of fractal dimension for geometrical multifractals. *Physica A: Statistical Mechanics and its Applications*. 1989;159(2): 155–166.
27. Viscek T. Mass multifractals. *Physica A: Statistical Mechanics and its Applications*. 1990;168(1): 490–497.
28. Lopes R, Betrouni N. Fractal and multifractal analysis: A review. *Medical Image Analysis*. 2009;13(4): 634–649.
29. Hilarov VL, Damaskinskaya EE. Fractal features of fracture centers in heterogeneous materials revealed by discrete element method. *Materialwissenschaft und Werkstofftechnik*. 2023;54(12): 1554–1559.
30. Lockner DA, Byerlee JD, Kuksenko V, Ponomarev A, Sidorin A. Quasi-static fault growth and shear fracture energy in granite. *Nature*. 1991;350: 39–42.
31. Hilarov VL. Self-Similar crack generation effects in the fracture process in brittle materials. *Modeling Simul Mater Sci Eng*. 1998;6: 337–342.